Journal of Zhejiang University-SCIENCE A (Applied Physics & Engineering) in press
www.jzus.zju.edu.cn; www.springer.com/journal/11582
E-mail: jzus_a@zju.edu.cn

Research Article

https://doi.org/10.1631/jzus.A2400478

Study of finite element model updating methodology and application to flexible resonance of high-speed railway vehicles

Chao CHANG[1,2,3], Liang LING[2]✉, Xiaoyi MA[1], Fansong LI[2], Tao LIU[3], Wanming ZHAI[2]

[1]*School of Mechatronics and Vehicle Engineering, East China Jiaotong University, Nanchang 330013, China*
[2]*State Key Laboratory of Rail Transit Vehicle System, Southwest Jiaotong University, Chengdu 610031, China*
[3]*CRRC Changchun Railway Vehicles Co., Ltd., Changchun 130000, China*

Abstract: The flexible resonance phenomenon of a carbody greatly affects the stability and safety of high-speed trains. Therefore, an accurate finite element (FE) model is crucial for establishing a rigid-flexible multi-body dynamics model and revealing the flexible resonance mechanism of high-speed trains. In this paper, we introduce an effective calibration and validation methodology for a carbody FE model of high-speed trains based on experimental modal analysis (EMA). A detailed three-dimensional (3D) carbody FE model that considers practical constraints was developed, and the carbody material parameters were optimized using a genetic algorithm (GA). Based on the updated model, a high-speed railway vehicle-track rigid-flexible coupled dynamics model was established. Results showed excellent agreement between the numerical simulations and field measurements. The proposed method was able to accurately reproduce the carbody flexible resonance phenomenon and elastic modal frequency observed on site.

Key words: High-speed train; Carbody flexible resonance; Finite element; Model updating; Modal frequency.

Unedited

1 Introduction

The high-speed train (HST) has emerged as a highly effective mode of transport for journeys of medium to long distances, offering high levels of comfort, speed, and efficiency. As HSTs have increased in running speed, the need for lighter carbody structures has intensified, which can result in diminished stiffness and reduced frequencies of the lower-order elastic modes of the carbody. Concurrently, this rise in velocity has introduced several issues, including increased wheel-rail wear, reduced stability during operation, and heightened abnormal vibrations in the vehicles. The resonance phenomenon, particularly that caused by elastic deformation of the carbody, has been linked to decreased passenger comfort and compromised operational safety (Jing et al., 2021; Wei et al., 2017; Huang and Zeng, 2021). Moreover, the human body is highly perceptive to vertical vibrations within the 4 to 8 Hz range, which coincides with the frequency band of abnormal resonances observed in the carriage (UIC and CEN, 1994).

To precisely capture the carbody's elastic deformation characteristics, the development of a dynamic model is essential, which necessitates the creation of an exceptionally precise finite element (FE) model. The practice of model updating is widely used across various disciplines such as structural health monitoring, aerospace, automotive, and civil engineering to validate and refine the accuracy of FE models (Simoen et al., 2015; Chang et al., 2022). FE model updating constitutes a mathematical procedure where the initial model's assumptions and parameters are incrementally adjusted to achieve convergence. The main approach to FE model updating involves using experimental test data to ascertain the structural modal parameters, which are then compared with the model's predictions to

✉ Liang LING, liangling@swjtu.edu.cn
Chao CHANG, https://orcid.org/0000-0002-9671-6673
Liang LING, https://orcid.org/0000-0002-9574-4875

Received Oct. 16, 2024; Revision accepted Apr. 17, 2025; Crosschecked

© Zhejiang University Press 2025

facilitate the updating process. Typically, this involves the use of data such as acceleration time histories, frequency response functions (FRFs), natural frequencies, modal displacements, modal strains or curvatures, and modal deflections, all of which are collected during experimental testing to inform the FE model updates (Alkayem et al. 2018).

However, FE model updating is a problematic and ill-conditioned inverse problem. Current FE model updating methods include: sensitivity-based function methods (Rezaiee-Pajand et al.,2021; Zhu et al. 2021), Bayesian updating methods (Mukesh et al., 2022; Sadri et al., 2016), component mode synthesis techniques (Papadimitriou and Papadioti, 2013), a response function method (Arora, 2011) and a power spectral density (PSD) based strategy (Pedram et al., 2017). In recent years, more and more scholars have chosen to apply optimization algorithms to model updating. Several studies (Tran-Ngoc et al., 2021; Girardi et al., 2021; Jung and Kim, 2013; Xiong and Lian, 2021) adopted a global optimization algorithm to realize the modal modification of large structures. The research showed that an optimization algorithm has the advantages of strong adaptability, high search efficiency and high accuracy.

Over recent decades, academics have proposed a variety of enhanced simulation models of tracks or infrastructures to analyze the vibration induced by wheel-rail interactions (Paixão et al., 2014; Malveiro et al. 2018). Modal identification and verification for railway bridges or tracks are based mainly on field measurements, using excitation methods such as impact loading (Ticona Melo et al. 2020), passing trains (Szafrański, 2021), or ambient excitation (Jiang, H et al., 2021). However, a vehicle system model allows more flexibility and can be used for both indoor test modal analysis (EMA) and outdoor operation modal analysis (OMA). Several studies (Silva et al., 2021; Ribeiro et al.,2021, 2022; Bragança et al., 2021) have described research on updating FE models of railway freight wagons. Compared with the results of freight wagon dynamic tests, an updated model has higher accuracy. The current model updating techniques have achieved good results for wagon models.

A passenger vehicle presents a significantly higher level of complexity and an expanded array of parameter variables than a wagon, which complicates the creation of an FE model that accurately mirrors the actual structure. Despite this, researchers have devised diverse strategies to tackle this difficulty. Using a particle swarm optimization algorithm, genetic algorithms (GA), and data from indoor modal tests, Akiyama et al. (Akiyama et al., 2020) and Ribeiro et al. (Ribeiro et al., 2013) crafted a simplified FE model with reduced mesh density and successfully updated the FE model for high-speed train carriages. You (You et al., 2021) proposed an updating method that relies on measured FRFs to modify an HST carbody FE model, incorporating a Kriging surrogate model with multi-objective functions for optimization and calibration with the revised parameter values. Montenegro et al. (Montenegro et al., 2015) and Molodova et al. (Molodova et al., 2014) concentrated on enhancing a wheel-rail contact model for passenger vehicles to achieve greater precision in vehicle-track coupled dynamics and wheel-rail high-frequency interactions. Despite the advancements from these studies, the following limitations remain in the context of FE model updating for HST passenger carbodies:

The existing railway passenger carbody FE models are relatively simple, and it is difficult to reflect the local vibration characteristics of the carbody structure. For instance, when detailed observations of deformation patterns, orientations, and other dynamic characteristics of specific structural components, such as the underframe and side walls of the carbody, are required for a particular modal shape, simplified FE models typically fail to deliver sufficient accuracy.

HSTs generally have various types of equipment placed underneath the underframe, which are connected by means of elastic or rigid connections. The arrangement of equipment and the connection parameters have been shown to affect the modal results of the vehicle (Gong et al.,2019).

The engineering problem of abnormal elastic vibration of the carbody due to poor wheel-rail matching, deterioration of bogie suspension components, and wheel polygonization presents significant challenges. Despite much research, a comprehensive mechanism for theoretical simulation of this vibration phenomenon has yet to be developed. As a result, an updated carbody FE model has been applied only rarely in relevant scenarios (Shi and Wu,

Unedited

2016; Sun et al., 2021).

The aim of this study was to develop an effective calibration and validation method for a carbody FE model of HSTs based on EMA to establish a rigid-flexible multi-body dynamics model and reveal the flexible resonance mechanism of HSTs. We aimed to accurately reproduce the carbody flexible resonance phenomenon and elastic modal frequency observed on site. To achieve this goal, we set out to establish an accurate vehicle FE model by combining an optimization algorithm with modal test data.

The rest of this paper is structured as follows. The FE modelling of the HST carbody is presented in Section 2, which describes the numerical modeling technique in detail. In Section 3, we present the modal test on the carbody, including the test layout and parametric analysis. Section 4 shows the correction process of the model based on the GA and calibrates the accuracy of the model based on the modal assurance criterion (MAC) and frequency error indicators. An HST vehicle-track coupled dynamics model was constructed based on the updated carbody FE model, as detailed in Section 5. The carbody flexible vibration phenomena were reproduced for normal operation and resonance conditions. The findings and recommendations for additional research are presented in Section 6.

2 FE modelling of the HST carbody

2.1 Description of the HST carbody

This study focused on a new generation of Chinese passenger HSTs operating at a maximum speed of 350 km/h. The HST features a distributed traction configuration comprising four motor vehicles and four trailers. Taking a trailer as an example, Fig. 1 shows a schematic diagram of the carbody. The carbody (trailer carriage) in service, including internal equipment, fittings, and other components, has a total mass of 41.03 tons under no-load conditions and 45.89 tons under normal load conditions. From both side and plan views, the length of the vehicle is 25.0 m (Fig. 1a). The wheelbase is 2.5 m long, and the distance between the pivots of the bogies is 17.8 m. Fig. 1b shows the cross-section and structural details of the carbody.

As shown in Figs. 1a-1b, the carbody includes not only the aluminum alloy shell but also internal fittings and various equipment positioned underneath and inside. The carbody shell is made of large, hollow, thin-walled aluminum alloy extrusion profiles that can be mechanically welded on a large scale.

Unedited

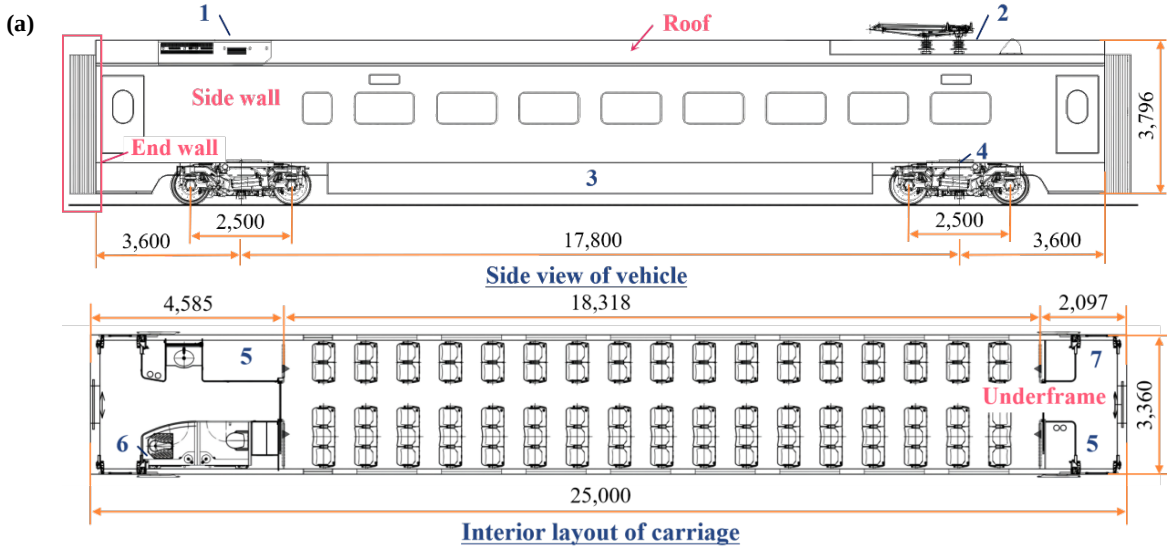

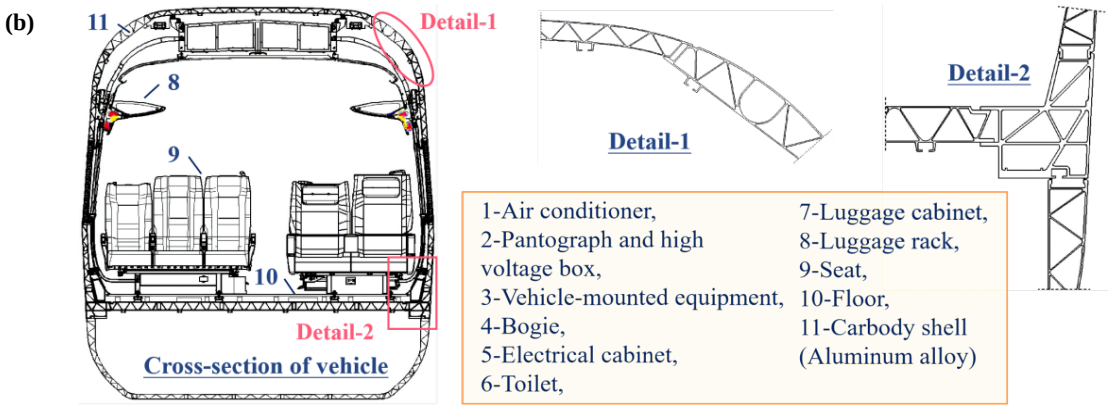

Fig. 1 HST trailer carbody: (a) Side and plan views (dimensions in mm); (b) Cross-section and structural details

Fig. 2 compares actual photographs of the cabody shell with the fully equipped carbody in service. The fully equipped carbody weighs between 40-45 tons, about four times heavier than the carbody shell (about 10 tons). This significant difference is due mainly to the additional components that make up the carbody in service, which include equipment under the carbody weighing 5-10 tons, an interior consisting of seats, windows, doors, luggage racks, and side wall panels weighing about 8 tons, and other components such as the air conditioning system, equipment cabinets, cables, and toilet modules that collectively weigh about 10 tons. Consequently, the modes of the carbody shell and the carbody in service exhibit stark contrasts. For example, the first modal frequency (f_{mode1}) of the empty carbody shell was measured to be 13.03 Hz, whereas the carbody in service exhibited a frequency of 8.73 Hz, yielding a frequency difference of about 33%. Other modal orders showed similar significant differences.

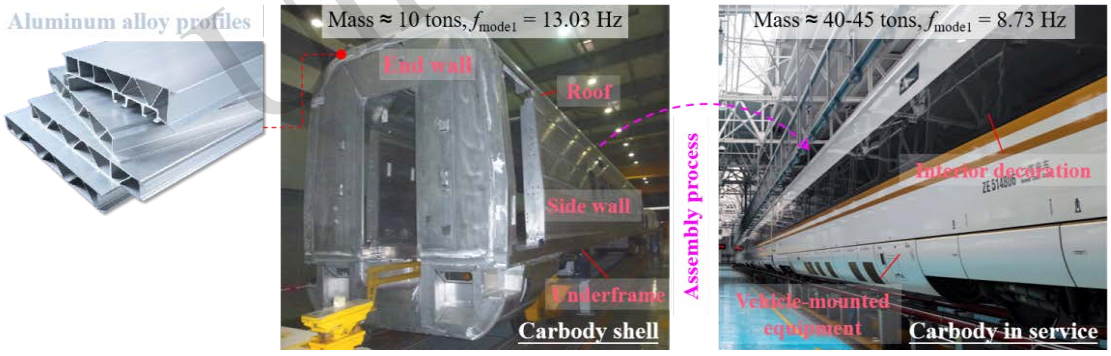

Fig. 2 Difference in appearance between the carbody shell and the carbody in service

Fig. 3 illustrates a schematic of the equipment installed under the carbody underframe. Fig. 3a shows the layout of the large-scale electrical and auxiliary equipment, whose mass varies from less than 1 ton to several tons, and is situated under the underframe. The equipment includes a sewage tank, auxiliary converter, auxiliary compressor, traction transformer, and an air cylinder braking module. The various items of equipment are connected to the side beams of the underframe through either elastic or rigid hanging mechanisms. Elastic hanging devices are supplemented with damping materials, whereas rigid suspensions are directly connected by bolts (Fig. 3b).

Unedited

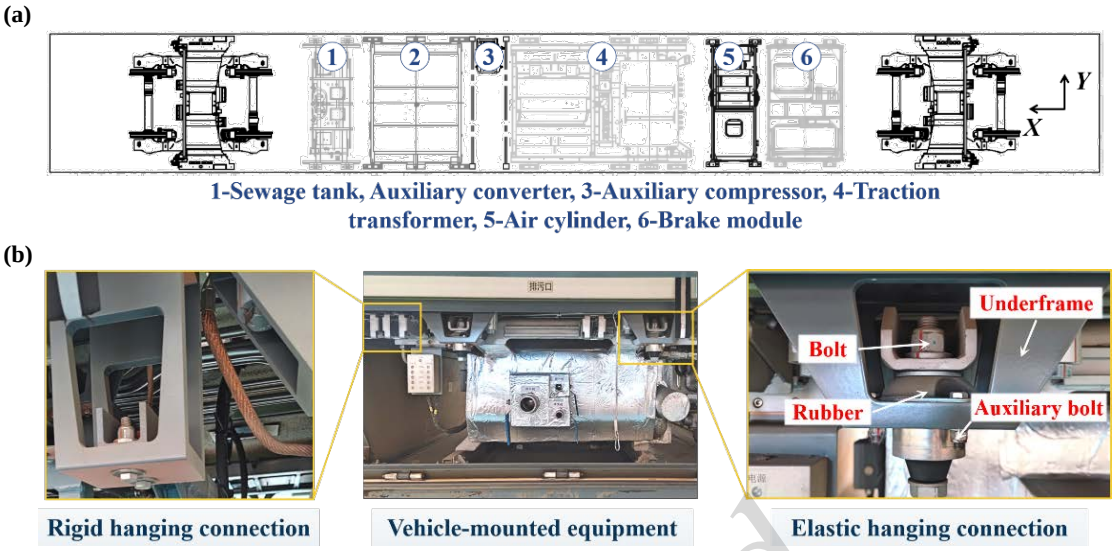

Fig. 3 Equipment under the carbody underframe: (a) Equipment layout; (b) Elastic hanging and rigid hanging connection

2.2 FE modeling of the HST carbody in service

Generally, an accurate model of a carbody shell of an HST can be obtained by the FE method. However, because the carbody is extremely complicated in operational service, there is a need to establish a more realistic FE model. In this study, we describe a method of creating the initial FE model in HyperMesh software. It is a pre-processing software for FE calculation (Zhang et al., 2008).

As shown in Fig. 4a, in accordance with the existing methods (Li et al., 2021, 2022), any distributed weight (such as internals and cables) located near the carbody shell was represented using

mass points that are attached to the structure. Additionally, any concentrated mass (such as large equipment) is hung on the carbody shell in a realistic connection mode. The FE model also incorporated the bogie bolsters and secondary suspension devices taking into account boundary constraints. For the bolster assembly, spring-damping elements (Combine14/39 elements) were introduced to account for the properties of the air springs, anti-yaw dampers, anti-rolling torsion bars, and lateral dampers within the secondary suspension system. Particular attention was given to the representation of heavy and bulky equipment, such as traction converters or brake modules, mounted on the vehicle.

It is imperative to model elastic or rigid connections at the appropriate locations on the underframe or roof (Fig. 4b). In this study, Mass21 elements were used to replicate the vehicle-mounted equipment, incorporating their mass and inertia characteristics. RBE3 and Combine14 elements were used to mimic the structural connections between the equipment. However, note that the shape of the equipment was not considered in the modeling process.

The model underwent a refinement process centered on the principle of equivalent stiffness (Chang et al.,2022; Li et al., 2022), accounting for the alterations in the carbody stiffness due to the presence of equipment and internal fittings. The carbody was segmented into four distinct zones according to the characteristics of the carbody shell structure: underframe, side walls, roof, and end walls. To emulate the increased stiffness contributed by doors and windows, coupling constraints were applied to these components. The carbody FE model was constructed with a total of 2,420,442 elements and 1,958,653 nodes, with shell elements dominating the composition. Note that the elastic modulus for the material in question was maintained as that of the aluminum alloy.

Unedited

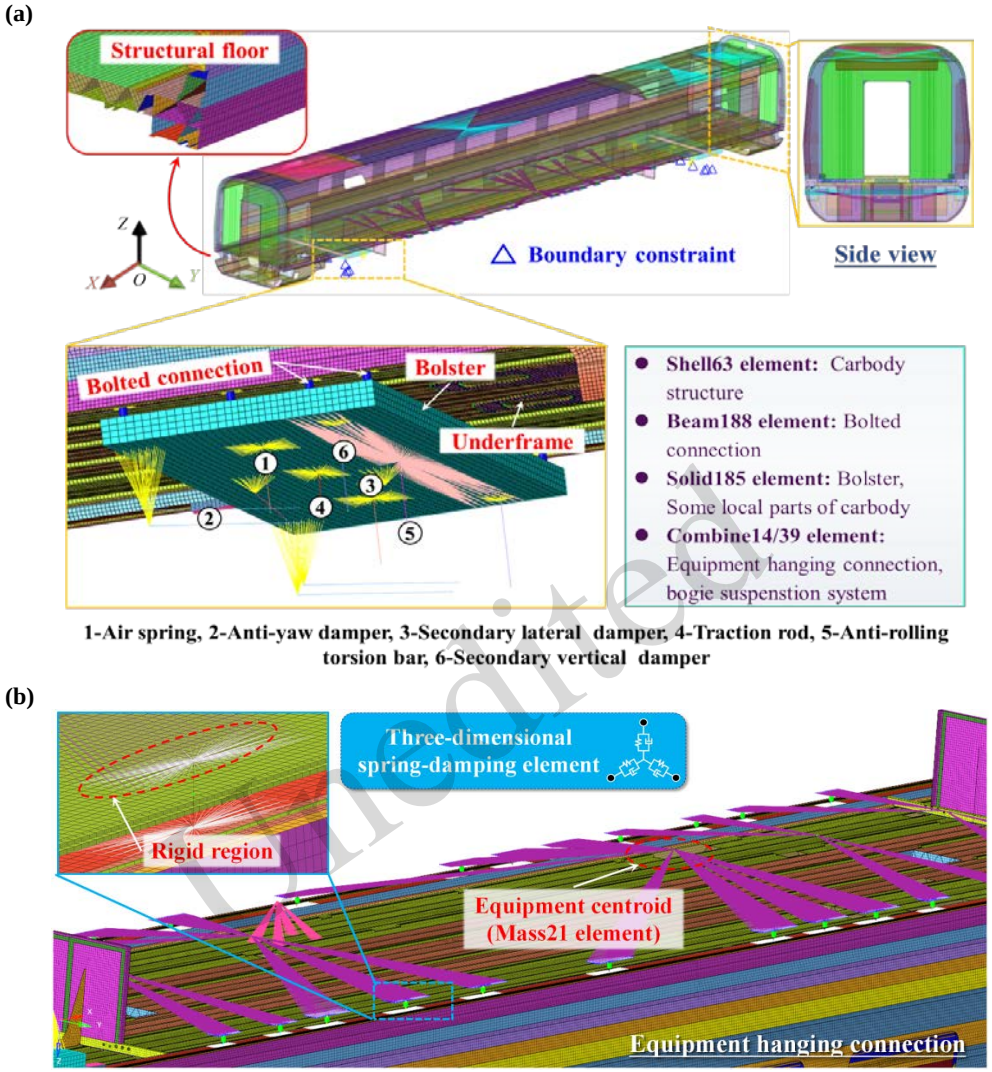

Fig. 4 Carbody FE model in operational service: (a) Overall view and secondary suspension simulation; (b) Finite element simulation of on-board equipment, explicitly showing elastic and rigid connection details

2.3. Modal analysis

Table 1 shows the material property parameters of the carbody FE model before calibration. The initial material parameters were determined according to the carbody shell materials used in the manufacturing process. The first six modal shapes and corresponding natural vibration frequencies prior to any adjustments are illustrated in Fig. 5, calculated and solved by means of ANSYS software using the Lanczos method. Essentially, this method combines the vector inverse iteration and Rayleigh-Ritz methods to transform the initial eigenvalue problem into a more manageable tridiagonal matrix eigenvalue problem within the Ritz vector space, also referred to as the Lanczos vector space in this context (Paige, 1972).

The presented modes essentially involve global movements of the carbody, some of them also incorporating local movements of the carbody structure. Modes 1-2 and 4 pertain to the bending vibration modes of the underframe of the vehicle, while Mode 3 is associated with the overall diamond vibration mode of the carbody. Mode 5 is related to the bending deformation of the underframe and the local deformation of the roof, while Mode 6 is focused on the torsional vibration mode of the carbody with simultaneous deformation of the underframe.

Table 1. The parameters of the carbody FE model before calibration

Parameter	Designation	Adopted value	Unit
E_u	Underframe's modulus	71.0	GPa
E_s	Side wall's modulus	71.0	GPa
E_r	Roof's modulus	71.0	GPa
E_e	End wall's modulus	71.0	GPa
ρ_u	Underframe's density	2700	kg/m^3
ρ_s	Side wall's density	2700	kg/m^3
ρ_r	Roof's density	2700	kg/m^3
ρ_e	End wall's density	2700	kg/m^3
μ_u	Underframe's poisson ratio	0.33	—
μ_s	Side wall's poisson ratio	0.33	—
μ_r	Roof's mpoisson ratio	0.33	—
μ_e	End wall's poisson ratio	0.33	—

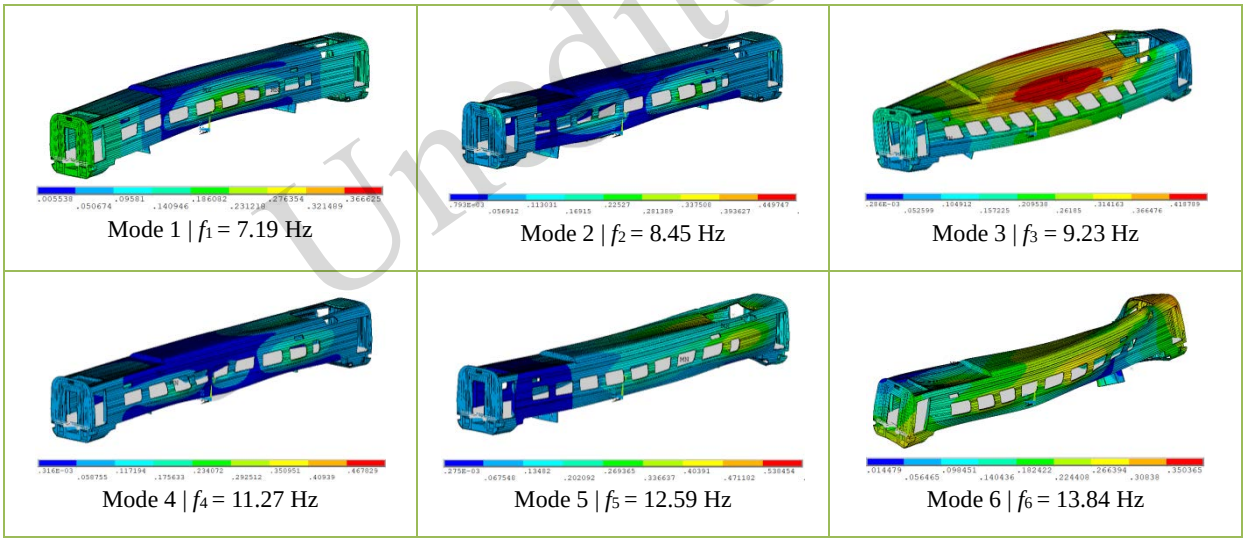

Fig. 5 Numerical modal parameters before calibration

Unedited

3 Modal test of the HST carbody

The objective of conducting a modal test on the operational HST carbody was to experimentally determine its modal parameters, which encompass the natural frequencies of vibration, corresponding mode shapes, and damping factors.

3.1 Measurement setup

The process of the modal test is shown in Fig. 6a. The carbody was supported on the bogies. The resolution of the acceleration sensor was 0.0001g rms, and the sensitivity of the force sensor was 2.2 mV/N. The excitation force applied in the modal test was provided by an electric vibration exciter capable of generating burst random signals. The excitation force amplitude was controlled to ensure a stable, broadband excitation in the frequency range of interest (0–64 Hz). The exciter applied excitation at two carefully selected points on the carbody floor structure, chosen to avoid modal node locations. Analysis bandwidth was also 0-64 Hz, the number of

spectral lines was 1024, and frequency resolution was 0.0625 Hz. The force signal source was burst randomly.

In addition, the reciprocity test needs to be completed. Selecting two excitation points, concentrated on the carbody floor hard skeleton position. Reciprocity testing in modal analysis is essential to verify the consistency and reliability of measured FRF. In the measurement of the two-input multiple-output FRF, the self-power spectrum and the mutual power spectrum were used to calculate the FRF based on the average number of 26 sampling times. The floor was flat and there were no vibration sources in the vicinity.

The carbody was arranged with 196 measurement points. Fig. 6b shows the arrangement of the measurement points for the modal test, with the direction of the measurement points defined by the carbody coordinate system. The modal experimental data were obtained by moving the acceleration sensors. There are 14 sensors within a single section. As the carbody structure is made up of the main frame structure and individual panels, the principle of the measurement points arrangement was divided into two parts. The first part was on the main carbody frame, on the bottom longitudinal beam of the carbody. The second part was on each main panel, floor and roof.

Unedited

(a)

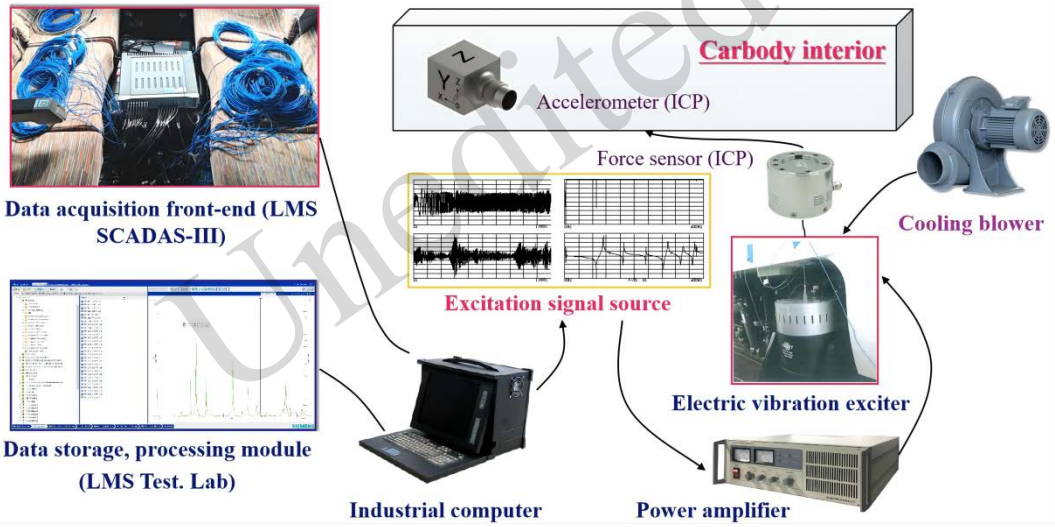

(b)

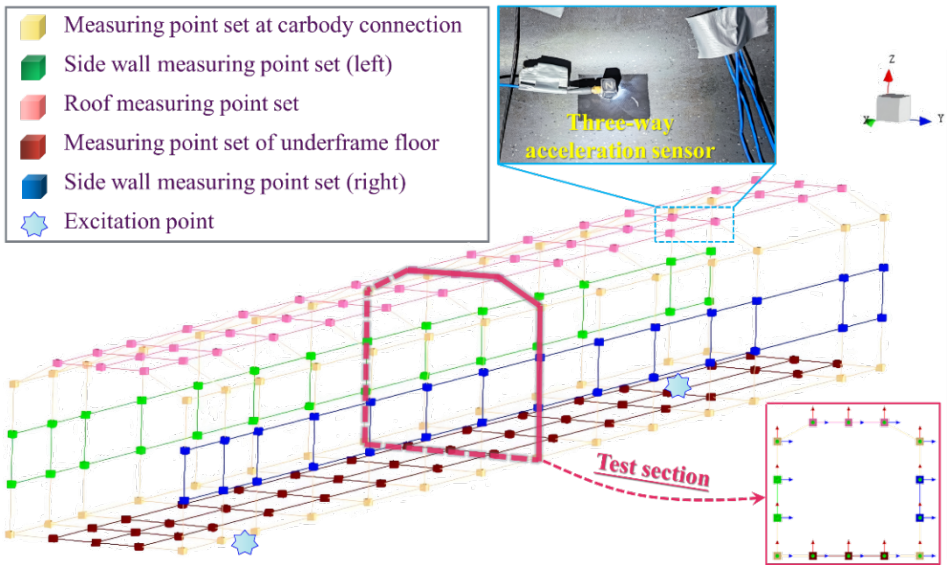

Fig. 6 (a) The flowchart of the carbody modal test; (b) Layout of measuring points

3.2 Modal parameter identification

The modal parameters for the carbody were identified by the application of the PolyMAX method implemented in the LMS software. The theoretical basis of the PolyMAX method is the Least Square Complex Frequency (LSCF) domain method (Peeters et al., 2004). The solving process is as follows: 1) The steady state diagram is determined by establishing a linear direct intersection matrix fractional model to determine the real modal frequency, damping and participation factor (Eqs (1)-(3)). 2) Obtaining poles and modal participation factors (Eq. (4)). 3) Least Squares Frequency Domain Method (LSFD) for modal analysis (Eq. (5)).

$$[\boldsymbol{H}(w)]=[\boldsymbol{B}(w)][\boldsymbol{A}(w)]^{-1}, \tag{1}$$

$$\begin{cases}[\boldsymbol{B}(w)]=\sum_{r=0}^{p}\boldsymbol{Z}(w)^r[\boldsymbol{\beta}_r],\\ [\boldsymbol{A}(w)]=\sum_{r=0}^{p}\boldsymbol{Z}(w)^r[\boldsymbol{\alpha}_r].\end{cases} \tag{2}$$

where w is the modal nature frequency, $\boldsymbol{H}(w)$ represents the FRFs, $\boldsymbol{B}(w)$ is the output parameter channel matrix, $\boldsymbol{A}(w)$ is the input parameter channel matrix; $\boldsymbol{\beta}$, $\boldsymbol{\alpha}$ are the polynomial coefficients of the numerator and denominator matrix, and r is the order of the mathematical model, set from 0 to p. $\boldsymbol{Z}(w)$ is an elementary item of the polynomial, which can be expressed as

$$\boldsymbol{Z}(w)=\mathrm{e}^{-\mathrm{j}w\Delta t}, \tag{3}$$

where Δt is the sampling time.

$$\begin{bmatrix}[\mathbf{O}] & [\mathbf{I}] & [\mathbf{O}] & \cdots & [\mathbf{O}]\\ [\mathbf{O}] & [\mathbf{O}] & [\mathbf{I}] & \cdots & [\mathbf{O}]\\ \vdots & \vdots & \vdots & \ddots & \vdots\\ -[\alpha_0] & -[\alpha_1] & -[\alpha_2] & \cdots & -[\alpha_{p-1}]\end{bmatrix}\begin{bmatrix}[\mathbf{V}]\\ [\boldsymbol{\Lambda}][\mathbf{V}]\\ [\boldsymbol{\Lambda}]^2[\mathbf{V}]\\ \vdots\\ [\boldsymbol{\Lambda}]^p[\mathbf{V}]\end{bmatrix}=\begin{bmatrix}[\mathbf{O}]\\ [\mathbf{O}]\\ \vdots\\ [\mathbf{O}]\end{bmatrix}, \tag{4}$$

Where Λ is the eigenvalue matrix (diagonal matrix) and **V** is the eigenvector matrix.

$$\boldsymbol{H}(w)=\sum_{i=1}^{S}\left[\frac{\boldsymbol{\psi}_i\boldsymbol{l}_i^T}{\mathrm{j}w-\lambda_i}+\frac{\boldsymbol{\psi}_i^*\boldsymbol{l}_i^T}{\mathrm{j}w-\lambda_i^*}\right]-\frac{\boldsymbol{LR}}{w^2}+\boldsymbol{UR}. \tag{5}$$

where $\boldsymbol{\psi}_i$ is the ith-order modal vibration mode and $\boldsymbol{l}_i$ is the ith-order modal participation factor. N is the number of modes, λ_i is the pole, and $\boldsymbol{LR}$, $\boldsymbol{UR}$ are the lower and upper residual items. T denotes transpose.

The FRF data were selected based on clear FRFs and coherence close to 1 in the test frequency band. The parameter estimation frequency range was chosen within this band, with no more than 10 system poles. To minimize out-of-band effects, the start and end points of the selected frequency band were set to the minimum values. When estimating the number of poles, the measured FRFs of the selected points were summed by amplitude. Modal model verification first checks the exciter's fixation, sensor calibration, and signal quality. The obtained FRFs are verified by coherence, then compared with the reconstructed FRFs from modal parameter estimation in LMS software, considering the upper and lower residuals.

The second step was to determine the correctness of each estimate in the same group according to the MAC indicator. The MAC evaluates the spatial intersection of the two modes by evaluating the size of the elements on the non-diagonal line. In addition to the MAC indicator, we used the modal phase collinearity (MPC) indicator with the MAC. The MPC is a measure of the degree to which the modal phases of the measured responses at different points on a structure are collinear or aligned with each other (Carne and Dohrmann, 1994). The MPC can be used to evaluate the consistency of the measured modal parameters across different measurement locations. Both MPC and MAC indicators are important for ensuring the rationality of modal testing, and should be used together to provide a more comprehensive evaluation of the modal testing results.

MAC expresses the correlation between modal shape vectors, and the expression is as follows:

$$\mathrm{MAC}\left(\boldsymbol{\psi}_j^m,\boldsymbol{\psi}_l^m\right)=\frac{\left|\left(\boldsymbol{\psi}_j^m\right)^*\boldsymbol{\psi}_l^m\right|^2}{\left(\left(\boldsymbol{\psi}_j^m\right)^*\boldsymbol{\psi}_j^m\right)\left(\left(\boldsymbol{\psi}_l^m\right)^*\boldsymbol{\psi}_l^m\right)},\quad j\neq l \tag{6}$$

where $(\boldsymbol{\psi}_j^m)^*$ denotes the complex conjugate transpose of $\boldsymbol{\psi}_j^m$, and $\boldsymbol{\psi}_j^m$, $\boldsymbol{\psi}_l^m$ represent the modal shape vectors, respectively. The more linearly the two sets of vectors ($\boldsymbol{\psi}_j^m$, $\boldsymbol{\psi}_l^m$) are related, the closer the MAC is to 1, which indicates that the j-th measured mode shape is the same as the l-th measured mode shape, otherwise, the lower the correlation.

The MPC indicator is the linear relationship between the real part and the imaginary part of each

Unedited

element of the mode vector of the scaleless mode. For the real regular mode, the MPC should have a high value, usually close to 100%. The MPC can be calculated by the following equation (Reynders et al., 2012):

$$\mathrm{MPC}(\boldsymbol{\psi}_j)=\frac{\left\|\mathrm{Re}(\tilde{\boldsymbol{\psi}}_j)\right\|_2^2+\frac{1}{\varsigma_{\mathrm{MPC}}}\mathrm{Re}(\tilde{\boldsymbol{\psi}}_j^T)\mathrm{Im}(\tilde{\boldsymbol{\psi}}_j)\left[2(\varsigma_{\mathrm{MPC}}^2+1)\sin^2(\theta_{\mathrm{MPC}})-1\right]}{\left\|\mathrm{Re}(\tilde{\boldsymbol{\psi}}_j)\right\|_2^2+\left\|\mathrm{Im}(\tilde{\boldsymbol{\psi}}_j)\right\|_2^2}, \quad (7)$$

$$\varsigma_{\mathrm{MPC}}=\frac{\left\|\mathrm{Im}(\tilde{\boldsymbol{\psi}}_j)\right\|_2^2-\left\|\mathrm{Re}(\tilde{\boldsymbol{\psi}}_j)\right\|_2^2}{2\,\mathrm{Re}(\tilde{\boldsymbol{\psi}}_j)\mathrm{Im}(\tilde{\boldsymbol{\psi}}_j)}, \quad (8)$$

$$\theta_{\mathrm{MPC}}=\arctan\left[\left|\xi_{\mathrm{MPC}}\right|+\mathrm{sign}(\varsigma_{\mathrm{MPC}})\sqrt{1+\varsigma_{\mathrm{MPC}}^2}\right]. \quad (9)$$

After carrying out a thorough analysis and observation of the vibration mode, we were able to determine the effective mode model for the project. The MAC and MPC values obtained from the modal test (Fig. 7a-7b, respectively) were compared against engineering standards. The MAC indicator was considered relevant if greater than 0.7, and irrelevant if less than 0.1. Off-diagonal terms in the MAC matrix were observed to be less than 0.1, satisfying the discrimination criterion. Similarly, the MPC indicator had to be above 90%, which was met by the test results. To select the appropriate excitation points for the carbody, we carried out pre-tests and compared the results obtained from different points. Reciprocity tests were then conducted. Fig. 7c shows a comparison of the Z-direction frequency response function of the H_2 measuring point when excitation point 1 is excited and the H_1 measuring point when excitation point 2 is excited. These results met the reciprocity requirements.

Unedited

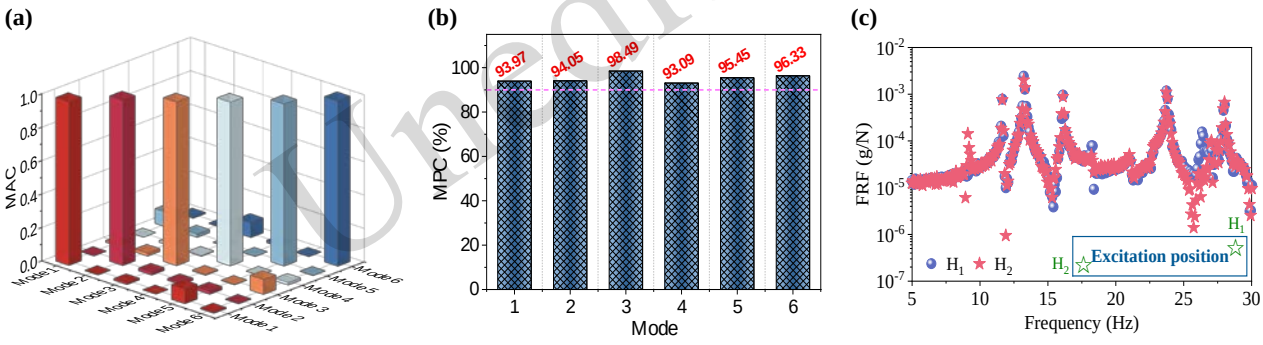

Fig. 7 Verification and analysis of modal test results: (a) MAC indicator; (b) MPC indicator; (c) Reciprocity test of excitation points

Fig. 8a presents the full FRFs at the observation point, enabling the distinct identification of the frequency associated with the carbody overall vibration mode. Fig. 8b shows the configurations of six identified vibration modes of the carbody, showcasing the mean values for natural frequencies and damping ratios. The deformed modal shapes are depicted with colored lines, while the undeformed mesh is shown in grey.

Mode 1 corresponds to the carbody first-order diamond vibration mode. Mode 2 represents the first-order bending of both the floor and roof. Mode 3 is characterized by the first-order vertical bending of the entire carbody. Mode 4 involves the second-order lateral bending of the underframe and roof, in conjunction with the second-order vertical side wall bending. Mode 5 is a combination of the first-order torsion and the first-order lateral bending. Mode 6 comprises the second-order torsion combined with the second-order lateral bending. The modal shape diagrams clearly show that the original, uncorrected carbody FE model significantly deviates from the experimental results, highlighting the need to refine the model.

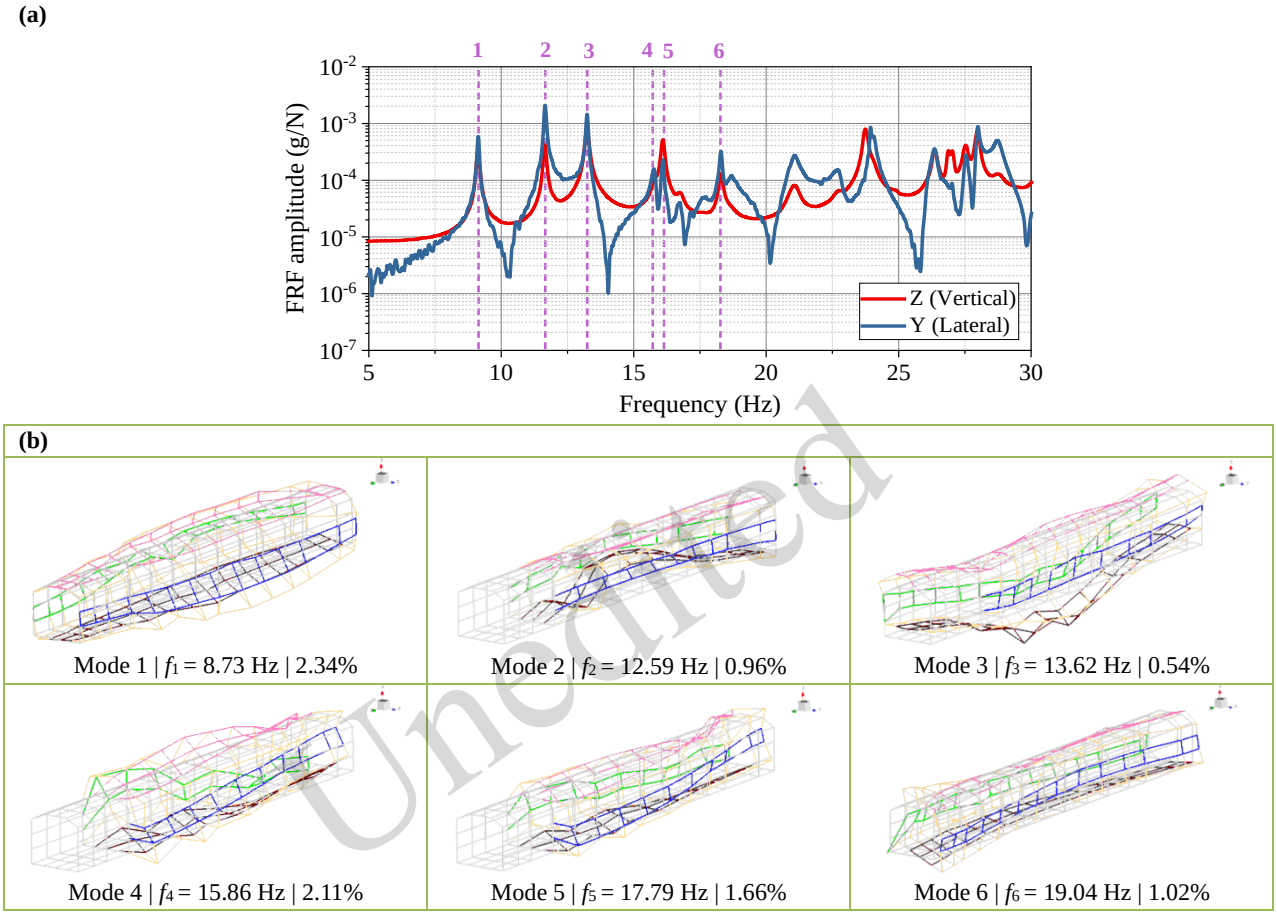

Fig. 8 (a) Identified modal parameters; (b) Experimental modal shapes of the carbody, with corresponding modal frequencies (Hz) and damping ratios (%) indicated for each mode

4 Calibration of carbody FE model

Section 4 describes how the refinement of the HST carbody FE model was carried out using the outcomes from the modal test, incorporating a sensitivity analysis and an optimization process that used a GA. The numerical and experimental mode shapes were automatically matched using the MAC, facilitating a comparative correlation analysis of the derived modal parameters.

4.1 Sensitivity analysis

A sensitivity analysis allows for selection of the numerical parameters (i.e. 6 natural frequencies, f_1 to f_6, and 6 MAC indicators, MAC1 to MAC6) that most influence the modal responses, and so should be included in the subsequent optimization stage. Twelve numerical parameters in Table 1 were selected, and random sampling was carried out using the latin hypercube sampling (LHS) method (Helton and Davis, 2003). LHS is a statistical technique used to generate a set of samples that are uniformly distributed over a specified range of values. The HyperMesh software completes the carbody FE model in service. According to Section 2, each region was given different material properties, accompanied by two bogie systems. The output was an ANSYS readable cdb format file. FE software ANSYS was used for modal analysis.

In the optimization process, only those parameters that are significantly correlated with the response can be correctly estimated. This can minimize

Unedited

the amount of calculation. The sensitivity analysis results are based on Spearman correlation coefficients r_{xy}^{S}, which express the correlation between two vectors of samples, x and y, based on their rank order vectors, $R(x_i)$ and $R(y_i)$, by the expression (Costa et al., 2016):

$$r_{xy}^{S}=\frac{\sum_{i=1}^{n}\left[R(x_i)-\bar{R}(x)\right]\left[R(y_i)-\bar{R}(y)\right]}{\sqrt{\sum_{i=1}^{n}\left[R(x_i)-\bar{R}(x)\right]^2\sum_{i=1}^{n}\left[R(y_i)-\bar{R}(y)\right]^2}}. \quad (10)$$

where $\bar{R}(x)$ and $\bar{R}(y)$ are the average values of the rank-order vectors $R(x_i)$ and $R(y_i)$, respectively, with i = 1, 2, ..., n, where n is the number of samples of each vector.

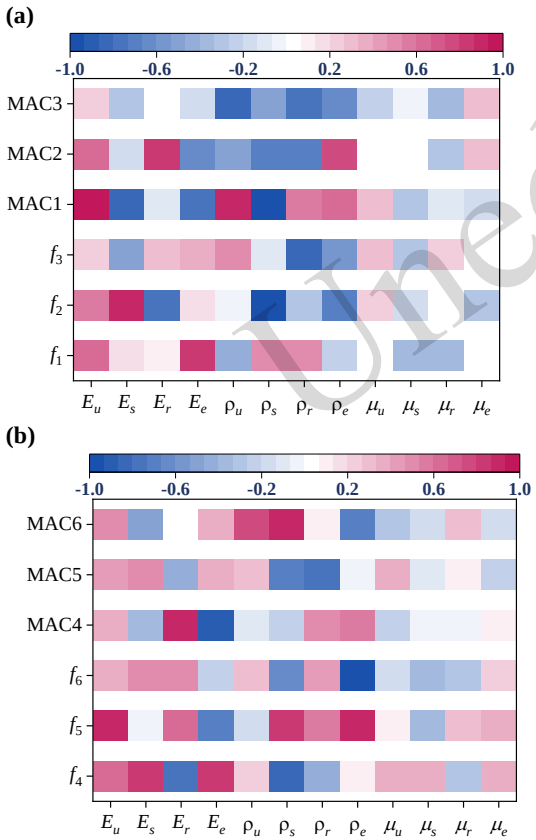

Fig. 9 Parameter sensitivity analysis: (a) MAC1-3, f_1-f_3; (b) MAC4-6, f_4-f_6

Fig. 9 shows the global sensitivity analysis results of 500 samples, based on the Spearman linear correlation matrix. To ensure the correct identification of parameters that have a significant impact on the modal response, samples with a MAC value below 0.50 were excluded from the total number of samples. This strategy proved effective in filtering out irrelevant samples. Continuing with the optimization stage, we considered only those parameters with a Spearman correlation coefficient above 0.50 that were associated with the modal response. The results of the sensitivity analysis show that the elastic modulus (i.e. E_u, E_s, E_r, E_e) and density parameters (i.e. ρ_u, ρ_s, ρ_r, ρ_e) of four regions, namely the underframe, the side wall, the roof and the end wall, were prominent in the modal response, while the Poisson's ratio had little effect.

4.2 Modal parameter optimization

The main objective of optimization is to determine the optimal value of a set of parameters identified through sensitivity analysis, to reduce the differences between simulation results and experimental results. To achieve this, a numerical model optimization process was initiated using a GA that requires the integration of two software packages, ANSYS and MATLAB. GA is an adaptive global optimization search algorithm, which simulates the process of biological heredity and evolution.

Fig. 10 outlines the iterative approach for updating the FE model. The GA was implemented within the MATLAB software framework, which interfaced with cdb files for conducting numerical simulations to assess natural frequencies and mode shapes. ANSYS-generated modal analysis data were transferred to MATLAB for modal pairing, where each experimental mode was matched with its numerical counterpart based on the highest MAC value. The GA then estimated a new set of numerical parameters, with the goal of reducing the residuals of the objective function. This iterative cycle was repeated until the predefined iteration limit was achieved. For the purposes of this research, binary coding was used, along with an initial population size of 50, a maximum evolutionary algebra of 50, and a generation gap of 0.9. The uniform crossover method was used, setting the crossover probability at 0.7 and the mutation probability at 0.05. The initial population was generated at random using LHS.

The upper and lower limits of the equivalent elastic modulus of the four regions are listed in Table 2, with their values set at 30 GPa and 150 GPa, respectively, to enable the GA to search for an optimal solution across a broad range (Li et al., 2022). Limits

Unedited

were also set when individual values within the population were updated and when these values exceeded the imposed limits. In reference to the optimization results, the density range of the four regions was set within 1000-10000 kg/m^3 to guarantee sufficient coverage during the search process.

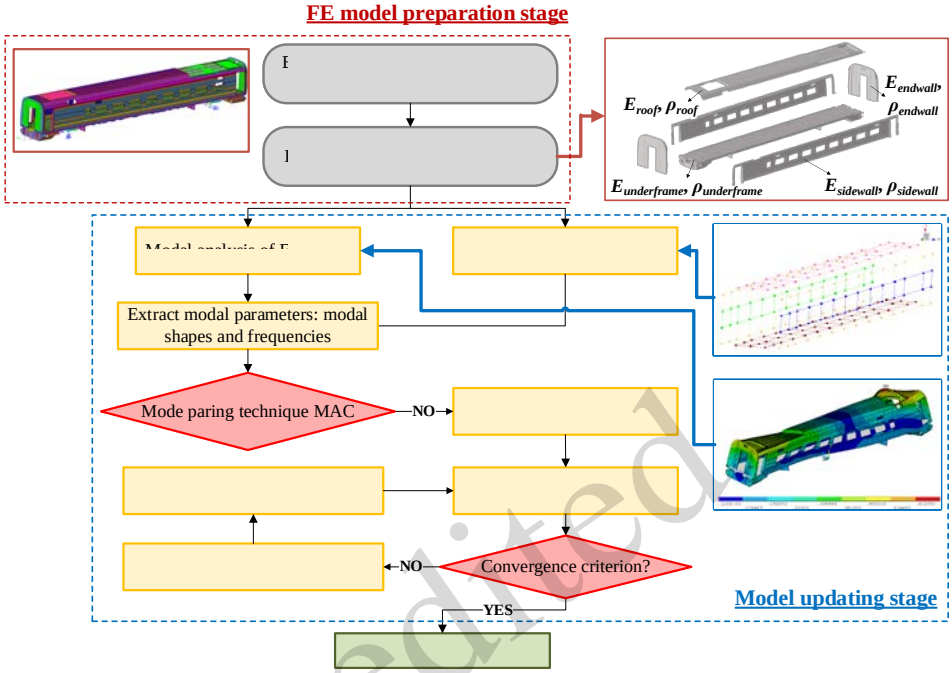

Fig. 10 The FE model updating process used in this study

Table 2. The parameters considered in the optimization analysis

Parameter	Designation	Initial value	Value range	Unit
E_u	Underframe's modulus	71.0	[30, 150]	GPa
E_s	Side wall's modulus	71.0	[30, 150]	GPa
E_r	Roof's modulus	71.0	[30, 150]	GPa
E_e	End wall's modulus	71.0	[30, 150]	GPa
ρ_u	Underframe's density	2700	[1000, 10000]	kg/m^3
ρ_s	Side wall's density	2700	[1000, 10000]	kg/m^3
ρ_r	Roof's density	2700	[1000, 10000]	kg/m^3
ρ_e	End wall's density	2700	[1000, 10000]	kg/m^3

The objective function f includes two terms, one is related to the natural frequencies of global and local modes, and the other is related to the MAC indicator of global and local mode shapes:

$$f=\frac{100\alpha}{\sum_{i=1}^{n}\gamma_i}\sum_{i=1}^{n}\left(\gamma_i\left|\Delta f_i\right|\right)+\frac{100\beta}{n}\sum_{i=1}^{n}\left(1-\mathrm{MAC}\left(\varphi_i^a,\varphi_i^m\right)\right), \quad (11)$$

$$\Delta f_i=\frac{f_i^m-f_i^a}{f_i^m}. \quad (12)$$

where n is the number of modes to be corrected and α is the weight factor of modal frequency and experimental modal frequency error. β is the weight equation of the modal shape correction part. To distinguish the degree of participation of each mode in iterative calculation, a parameter γ was added to the equation, which represents the i-th mode weight factor, with values ranging from 0 to 1. For the mode order that is the key correction, the mode weight factor was 1.

In Eq. (11), the first part on the right-hand side aims to match the natural frequency of the model to

Unedited

that of the test as closely as possible. The second part modifies the model's modal function matrix. Research shows that α/β within the range of 2 to 10 yields satisfactory correction results. In this study, the value was set to 4, with an α value of 1 and a β value of 0.25. As a result, the convergence judgment value of the objective function f was typically 4.5 for each mode represented in Eq. (12). Fig. 11 presents the relationship between the number of iterations and the evaluation function value. As the population evolves to the 30th generation, the evaluation function under the optimal value gradually approaches the objective function value of 4.5.

The determined material parameters were as follows: E_u=112 GPa, E_r=55.2 GPa, E_s=66.4 GPa, and E_e=65.7 GPa. Notably, the equivalent elastic modulus for certain areas did not exceed the 69 GPa characteristic of the aluminum alloy, with numerous sites exhibiting lower elastic moduli. The value of E_u exceeded 69 GPa suggesting that the internal structure of the carbody enhances its operational stiffness. In contrast, the E_r, E_s, and E_e values, which were below 69 GPa, denote a reduction in stiffness in these specific sections. The final optimization result of the density parameters were updated as follows: ρ_u=9029.3 kg/m^3, ρ_s=6566.7 kg/m^3, ρ_r=7076.9 kg/m^3, ρ_e=5175.1 kg/m^3.

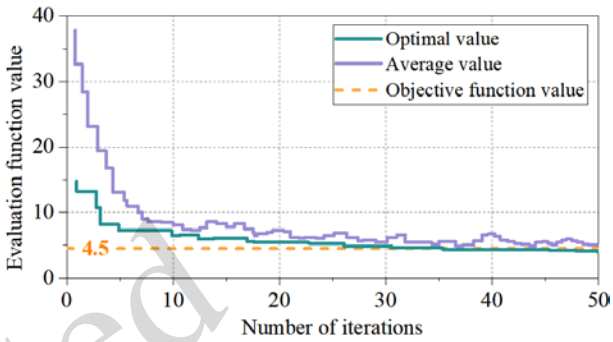

Fig. 11 Evaluation function value versus iterations during GA optimization

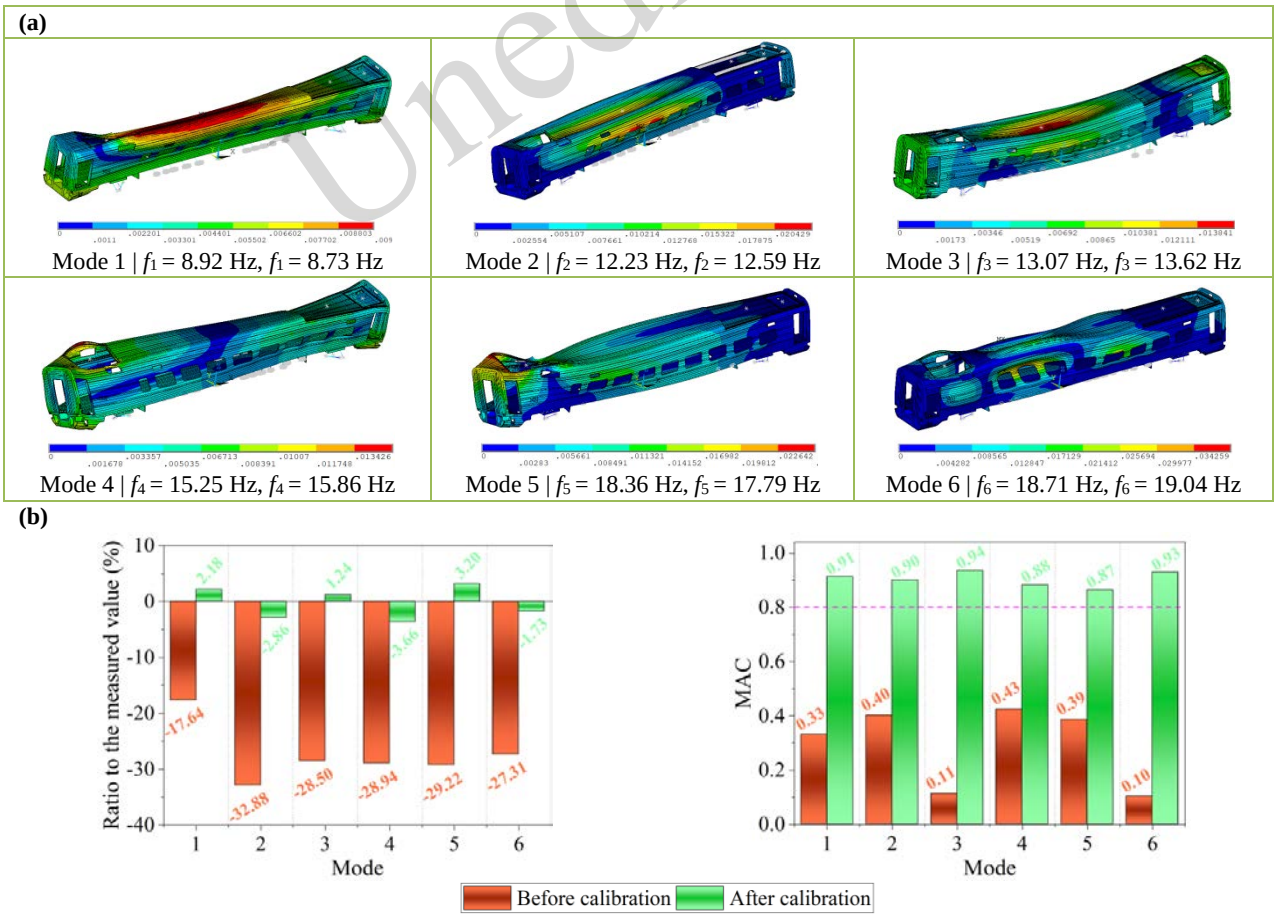

Fig. 12 (a) Comparison between the experimental (blue lines) and numerical simulation (red lines) modal shapes after FE

Unedited

model updating; (b) Errors between experimental and numerical modal responses, before and after calibration: Natural frequencies and MAC indicator

Fig. 12a presents a comparison of the experimental and calibrated numerical modal configurations. A marked resemblance between the numerical and experimental configurations was realized post-calibration. As shown in Fig. 12b, the MAC values were all greater than 0.8, and the absolute value of the relative error of each mode frequency was less than 5%. The accuracy of the updated FE model was obviously improved. Note that the prerequisite for revising the carbody FE model is to have experimental data as input, which is typically done after the initial product design is finalized. The updated model can then be used for fault identification, discussion of potential solutions, and ultimately optimizing the design of the product.

5 Application in the flexible resonance of a high-speed railway vehicle

Section 5 describes the application of the proposed model to the flexible resonance analysis of a high-speed railway vehicle. The dynamic responses obtained by the HST vehicle-track coupled model based on updated carbody FE model and the in-situ dynamic measurements are compared.

5.1 HST vehicle-track coupled model

The updated FE model was used to construct a rigid-flexible coupled dynamics model of the whole vehicle using both the vehicle-track coupled dynamics theory (Fig. 13) and Craig-Bampton modal synthesis method (Zhai, 2019; Boo et al., 2018). This vehicle system model comprises a flexible carbody, two bogies, five on-board pieces of equipment installed beneath the underframe, an air conditioning system on the roof, four wheelsets, two bolster beams, and eight axle boxes. The wheelset, frame, and other components with limited elastic deformation were treated as a rigid body. The bolster and underframe were rigidly connected. Maxwell models were used to calculate damping forces in the suspension systems, linear springs and dampers to mimic air springs and tailored elements to represent rubber components and bearings.

The dynamics of a slab ballastless track were treated as an object. The modeling of the track was based on the vibration theory of elastic thin plate, described in detail in reference (Zhai, 2019). The rail was simplified to a Timoshenko beam element. A full nonlinear non-Hertz Kik-Piotrowski model for wheel-rail normal contact was hired. It is a non-elliptical multi-point contact model based on the virtual penetration contact theory (Piotrowski and Kik, 2008). The FASTSIM algorithm was used to calculate the tangential stress distribution in the contact patch, and the wheel-rail tangential force was obtained by integration (Kalker, 1967, 1982; Sun et al., 2023).

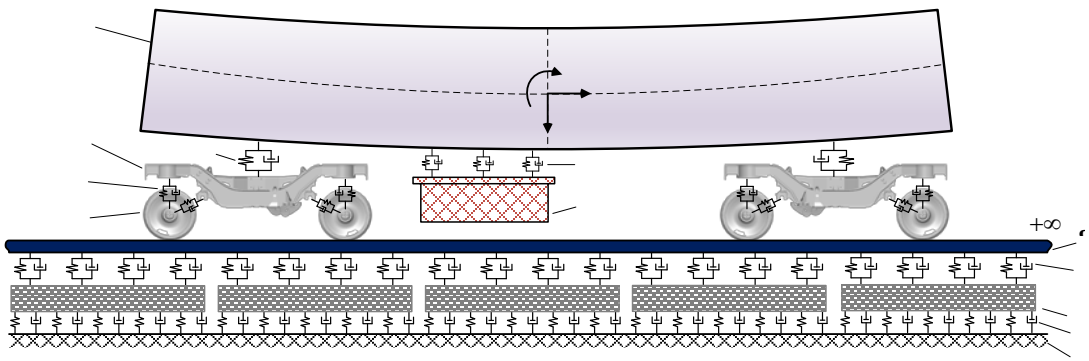

Fig. 13 Schematic view of the high-speed vehicle-track coupled dynamics model

5.2 Simulation of the flexible resonance of the high-speed vehicle

Unedited

Fig. 14 shows an abnormal condition of the ride comfort index in the middle floor of the vehicle carbody during a certain operation, with a maximum operation speed of 350 km/h. In this study, based on the Chinese railway specification GB/T 5599-2019 (Zhai, 2019), the Sperling index was selected for assessing ride comfort. When the Sperling index is greater than 3.0, it is considered unqualified. The vertical and lateral Sperling index exceeded the qualified line many times during operation, especially the vertical index, which had a maximum value of 3.93.

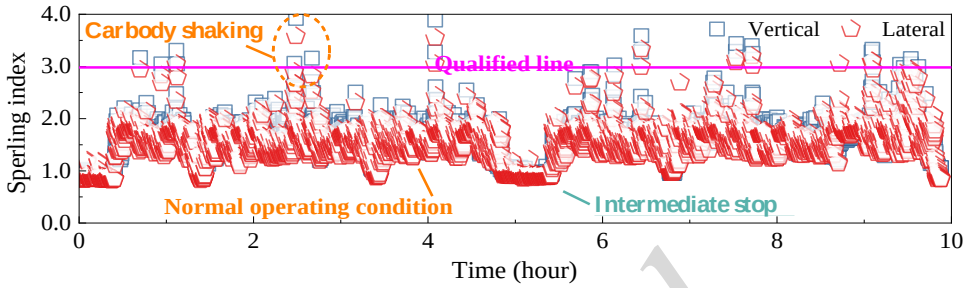

Fig. 14 Sperling index in the middle floor of an HST vehicle carbody

According to the feedback from the in-site test, in the time period when the Sperling indicator was abnormal, foot numbness can be obviously felt in the middle of the carbody floor, accompanied by the vibration phenomenon inside the carriage. The carbody shaking phenomenon appears to be similar to that described previously (Wei et al., 2017; Huang and Zeng, 2021; Shi and Wu, 2016) and may be caused by wheel-rail profile matching, abnormal disturbance of track irregularity in local areas, and other factors (Polach and Nicklisch, 2016).

Fig. 15 shows a simulation analysis of normal operation and carbody shaking conditions based on the rigid-flexible coupled dynamics model, with the display position in the middle of the carbody floor. The figure shows that the calculation results of the rigid-flexible coupled dynamics model established by the uncorrected carbody FE model are quite different from the test data. Especially under the shaking condition, the fluctuation in the time domain is significantly smaller than the test result. The main reason for this difference is that when the carbody FE model is not updated, the elastic frequency is far from the real modal frequency. The accuracy of the modified vehicle rigid-flexible coupled dynamics model was obviously improved.

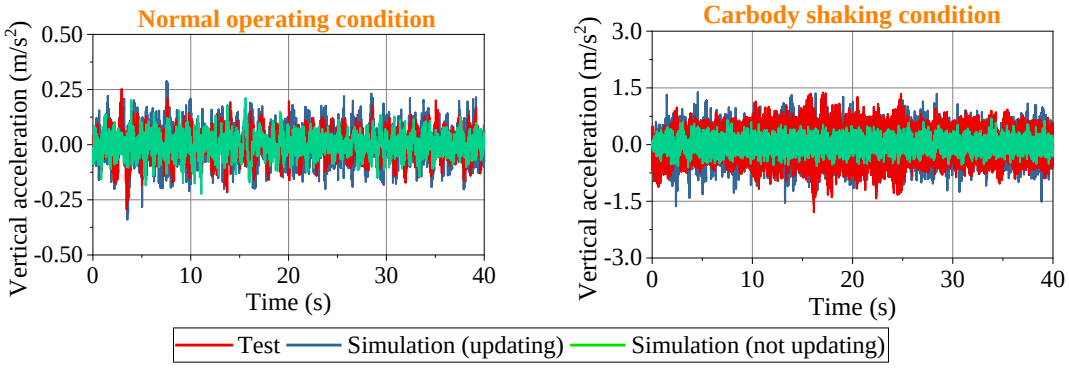

Unedited

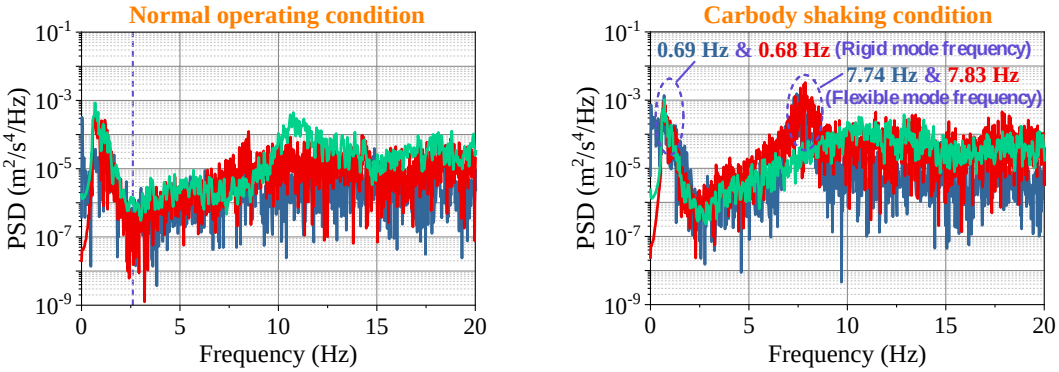

Fig. 15 Time histories and PSD diagrams of carbody middle floor accelerations under simulation (before and after updating) and test (350 km/h)

When carbody shaking appears, the vibration amplitude was about 3-4 times that of normal operation. It can be clearly seen from the PSD that there were obvious acceleration peaks at 0.68 Hz and 7.83 Hz in the frequency domain under the carbody shaking condition. Those frequencies correspond to the rigid body modal frequency and the first-order diamond modal frequency of the carbody, respectively. Because the test and analysis apply to the vehicle running at high speed, its frequency value is slightly different from the experimental modal frequency (f_1 = 8.73 Hz) (Orlowitz and Brandt, 2017). The simulation results are in good agreement with the test results and can reproduce the in-site response characteristics.

6 Conclusions and outlook

The main objective of this paper was to present a method for updating the carbody FE model using measured modal data. To create a comprehensive 3D numerical FE model of an HST carbody in service, different types of FE elements, including beam, shell, mass, and spring-damper, were used. The FE model was optimized and updated based on field modal tests. Numerical results were then used to verify the vertical movement of the carbody floor during specific working conditions of the train operation. Based on these findings, the following conclusions were drawn:

1. The calibration results indicated that the numerical simulation was consistent with the experimental measurements. Compared with the initial carbody FE model before calibration, the updated carbody FE model showed a significant improvement in the simulation of modal parameters. The frequencies obtained by updated model deviated slightly from the experimental frequencies, and the MAC indicators increased. The optimization results show that the material property parameters of the four regions of the carbody changed greatly compared with the aluminum alloy material, which is related to the service condition of the carbody

2. The HST vehicle-track coupled dynamics model was established by using the updated carbody FE model, and the dynamic response of the HST vehicle under normal operation conditions and flexible resonance conditions was simulated. The simulation results were in good agreement with the measured data, indicating that the updated carbody model accurately reflected the actual elastic resonance problem of the HST vehicle in the dynamic analysis.

Future work will focus on using the modified rigid-flexible coupled dynamics model to study how to deal with abnormal vibrations of HSTs, such as installing a dynamic vibration absorber beneath the underframe, and bogie active suspension control devices.

Acknowledgements

The authors wish to thank all the staff members involved in the test at the CRRC Changchun Railway Car Co., Ltd., Changchun, China. This work was supported by the State Key Laboratory of Rail Transit Vehicle System (Grant No. RVL2508); the National Natural Science Foundation of China [Grant No. 51735012, U19A20110, 52072317]; the Key Science and Technology Projects of CRRC (grant numbers 2020CYB147).

Author contributions

Chao CHANG designed the research. Chao CHANG and Xiaoyi MA processed the experimental and numerical data.

Unedited

Chao CHANG wrote the first draft of the manuscript. Fansong LI and Tao LIU helped to organize the manuscript. Liang LING and Wanming ZHAI revised and edited the final version.

Conflict of interest

Chao CHANG, Liang LING, Xiaoyi MA, Fansong LI, Tao LIU, and Wanming ZHAI declare that they have no conflict of interest.

References

Alkayem N F, Cao M, Zhang YF, et al., 2018. Structural damage detection using finite element model updating with evolutionary algorithms: a survey. *Neural Computing and Applications*, 30(2), 389-411. https://doi.org/10.1007/s00521-017-3284-1

Arora V. 2011. Comparative study of finite element model updating methods. *Journal of Vibration and Control*, 17(13), 2023-2039. https://doi.org/10.1177/1077546310395967

Akiyama Y, Tomioka T, Takigami T, et al., 2020. A three-dimensional analytical model and parameter determination method of the elastic vibration of a railway vehicle carbody. *Vehicle System Dynamics*, 58(4), 545-568. https://doi.org/10.1080/00423114.2019.1590606

Bragança C, Neto J, Pinto N, et al., 2021. Calibration and validation of a freight wagon dynamic model in operating conditions based on limited experimental data. *Vehicle System Dynamics*, 60(9), 3024–3050. https://doi.org/10.1080/00423114.2021.1933091

Brehm M, Zabel V, Bucher C. 2010. An automatic mode pairing strategy using an enhanced modal assurance criterion based on modal strain energies. *Journal of Sound and Vibration*, 329(25), 5375-5392. https://doi.org/10.1016/j.jsv.2010.07.006

Boo S H, Kim J H, Lee P S. 2018. Towards improving the enhanced Craig-Bampton method. *Computers & Structures*, 196, 63-75. https://doi.org/10.1016/j.compstruc.2017.10.017

Chang C, Ding X, Ling L, et al., 2022. Mechanism of high-speed train carbody shaking due to degradation of wheel-rail contact geometry. *International Journal of Rail Transportation*, 11(3), 289–316. https://doi.org/10.1080/23248378.2022.2077850

Carne T G, Dohrmann C R. 1994. A modal test design strategy for model correlation (No. SAND-94-2702C; CONF-950240-4). *Sandia National Labs.*, Albuquerque, NM (United States). http://dx.doi.org/10.4236/cs.2016.76070

Girardi M, Padovani C, Pellegrini D, et al., 2021. A finite element model updating method based on global optimization. *Mechanical Systems and Signal Processing*, 152, 107372. https://doi.org/10.1016/j.ymssp.2020.107372

Gong D, Duan Y, Wang K, et al., 2019. Modelling rubber dynamic stiffness for numerical predictions of the effects of temperature and speed on the vibration of a railway vehicle car body. *Journal of Sound and Vibration*, 449, 121-139. https://doi.org/10.1016/j.jsv.2019.02.037

Huang CH, Zeng J, 2021. Suppression of the flexible carbody resonance due to bogie instability by using a DVA suspended on the bogie frame. *Vehicle System Dynamics*, 60(9), 3051–3070 http://dx.doi.org/10.1080/00423114.2021.1930071

Helton J C, Davis F J. 2003. Latin hypercube sampling and the propagation of uncertainty in analyses of complex systems. *Reliability Engineering & System Safety*, 81(1), 23-69. https://doi.org/10.1016/S0951-8320(03)00058-9

Jing L, Wang KY, Zhai WM, 2021. Impact vibration behavior of railway vehicles: a state-of-the-art overview. *Acta Mechanica Sinica*. 37, 1193–1221. https://doi.org/10.1007/s10409-021-01140-9

Jung D. S, Kim C. Y. 2013. Finite element model updating on small-scale bridge model using the hybrid genetic algorithm. *Structure and Infrastructure engineering*, 9(5), 481-495. https://doi.org/10.1080/15732479.2011.564635

Jiang HW, Gao L, Zhao WQ. 2021. Model updating of the vehicle-track coupled system based on in-situ dynamic measurements. *Construction and Building Materials*, 298, 123861. https://doi.org/10.1016/j.conbuildmat.2021.123861

Kalker J. J. 1982. A fast algorithm for the simplified theory of rolling contact. *Vehicle System Dynamics*, 11(1), 1-13. https://doi.org/10.1080/00423118208968684

Kalker, J. J. 1967. On the rolling contact of two elastic bodies in the presence of dry friction.

Li FS, Wu H, Liu C, et al. 2022. Vibration fatigue analysis of high-speed railway vehicle carbody under shaking condition. *Vehicle System Dynamics*, 60(6), 1867-1887. https://doi.org/10.1080/00423114.2021.1880013

Li FS, Wu H, Wu PB. 2021. Vibration fatigue dynamic stress simulation under non-stationary state. *Mechanical Systems and Signal Processing*, 146, 107006. https://doi.org/10.1016/j.ymssp.2020.107006

Mukesh K, Rodrigo A, Ramin M, et al., 2022. Bayesian updating and identifiability assessment of nonlinear finite element models. *Mechanical Systems and Signal Processing*, 167, 108517. https://doi.org/10.1016/j.ymssp.2021.108517

Malveiro J, Sousa C, Ribeiro D, et al., 2018. Impact of track irregularities and damping on the fatigue damage of a railway bridge deck slab. *Structure and Infrastructure Engineering*, 14(9), 1257-1268. https://doi.org/10.1080/15732479.2017.1418010

Montenegro P. A, Neves S.G.M, Calçada R, et al., 2015. Wheel-rail contact formulation for analyzing the lateral train-structure dynamic interaction. *Computers & Structures*, 152, 200-214.

Uncorrected

https://doi.org/10.1016/j.compstruc.2015.01.004

Molodova M, Li ZL, Núñez A, et al., 2014. Validation of a finite element model for axle box acceleration at squats in the high frequency range. *Computers & Structures*, 141, 84-93.
https://doi.org/10.1016/j.compstruc.2014.05.005

Orlowitz E, Brandt A. 2017. Comparison of experimental and operational modal analysis on a laboratory test plate. *Measurement*, 102, 121-130.
https://doi.org/10.1016/j.measurement.2017.02.001

Papadimitriou C, Papadioti D C. 2013. Component mode synthesis techniques for finite element model updating. *Computers & structures*, 126, 15-28.
https://doi.org/10.1016/j.compstruc.2012.10.018

Pedram M, Esfandiari A, Khedmati M R. 2017. Damage detection by a FE model updating method using power spectral density: Numerical and experimental investigation. *Journal of Sound and Vibration*, 397, 51-76.
https://doi.org/10.1016/j.jsv.2017.02.052

Paixão A, Fortunato E, Calçada R. 2014. Transition zones to railway bridges: track measurements and numerical modelling. *Engineering structures*, 80, 435-443.
https://doi.org/10.1016/j.engstruct.2014.09.024

Paige C C. 1972. Computational variants of the Lanczos method for the eigenproblem. *IMA Journal of Applied Mathematics*, 10(3), 373-381.
https://doi.org/10.1093/imamat/10.3.373

Peeters B, Van der Auweraer H, Guillaume P, et al. 2004. The PolyMAX frequency-domain method: a new standard for modal parameter estimation? *Shock and Vibration*, 11(3-4), 395-409.
https://doi.org/10.1155/2004/523692

Piotrowski J, Kik W. 2008. A simplified model of wheel/rail contact mechanics for non-Hertzian problems and its application in rail vehicle dynamic simulations. *Vehicle System Dynamics*, 46(1-2), 27-48.
https://doi.org/10.1080/00423110701586444

Polach O, Nicklisch D. 2016. Wheel/rail contact geometry parameters in regard to vehicle behaviour and their alteration with wear. *Wear*, 366, 200-208.
https://doi.org/10.1016/j.wear.2016.03.029

Rezaiee-Pajand M, Sarmadi H, Entezami A. 2021. A hybrid sensitivity function and Lanczos bidiagonalization-Tikhonov method for structural model updating: Application to a full-scale bridge structure. *Applied Mathematical Modelling*, 89, 860-884.
https://doi.org/10.1016/j.apm.2020.07.044

Ribeiro D, Calçada R, Brehm M, et al., 2021. Calibration of the numerical model of a track section over a railway bridge based on dynamic tests. *Structures*, 34, 4124-4141.
https://doi.org/10.1016/j.istruc.2021.09.109

Ribeiro D, Bragança C, Costa C, et al., 2022. Calibration of the numerical model of a freight railway vehicle based on experimental modal parameters. *Structures*, 38, 108-122.
https://doi.org/10.1016/j.istruc.2022.01.085

Ribeiro D, Calçada R, Delgado R, et al., 2013. Finite-element model calibration of a railway vehicle based on experimental modal parameters. *Vehicle System Dynamics*, 51(6), 821-856.
https://doi.org/10.1080/00423114.2013.778416

Reynders E, Houbrechts J, De Roeck G. 2012. Fully automated (operational) modal analysis. *Mechanical systems and signal processing*, 29, 228-250.
https://doi.org/10.1016/j.ymssp.2012.01.007

SAC(Standardization Administration of the People's Republic of China), 2007, Reduced comfort boundary and evaluation criteria for human exposure to whole-body vibration, GB T 13441.1-2007. National Standards of the People's Republic of China.

Simoen E, De Roeck G, Lombaert G. 2015. Dealing with uncertainty in model updating for damage assessment: A review. *Mechanical Systems and Signal Processing*, 56, 123-149.
https://doi.org/10.1016/j.ymssp.2014.11.001

Sadri M, Brunskog J, Younesian D. 2016. Application of a Bayesian algorithm for the Statistical Energy model updating of a railway coach. *Applied Acoustics*, 112, 84-107.
https://doi.org/10.1016/j.apacoust.2016.05.014

Szafrański M. 2021. A dynamic vehicle-bridge model based on the modal identification results of an existing EN57 train and bridge spans with non-ballasted tracks. *Mechanical Systems and Signal Processing*, 146, 107039.
https://doi.org/10.1016/j.ymssp.2020.107039

Silva R, Ribeiro D, Bragança C, et al., 2021. Model updating of a freight wagon based on dynamic tests under different loading scenarios. *Applied Sciences*, 11(22), 10691.
https://doi.org/10.3390/app112210691

Shi, HL, Wu PB. 2016. Flexible vibration analysis for car body of high-speed EMU. *Journal of Mechanical Science and Technology*, 30(1), 55-66.
https://doi.org/10.1007/s12206-015-1207-6

Sun JF, Chi MR, Jin XS, et al., 2021. Experimental and numerical study on carbody hunting of electric locomotive induced by low wheel-rail contact conicity. *Vehicle System Dynamics*, 59(2), 203-223.
https://doi.org/10.1080/00423114.2019.1674344

Sun Y, Shi F F, Zhang S, et al., 2023. Improving the robustness of non-Hertzian wheel–rail contact model for railway vehicle dynamics simulation. *Multibody System Dynamics*, 1-45.
https://doi.org/10.1007/s11044-023-09903-x

Tran-Ngoc H, Khatir S, Le-Xuan T, et al., 2021. Finite element model updating of a multispan bridge with a hybrid metaheuristic search algorithm using experimental data from wireless triaxial sensors. *Engineering with Computers*, 38(3)1865-1883.
https://doi.org/10.1007/s00366-021-01307-9

Ticona Melo, L. R, Ribeiro D, Calçada R, 2020. Validation of a vertical train- track-bridge dynamic interaction model based on limited experimental data. *Structure and Infrastructure Engineering*, 16(1), 181-201.

Unedited

https://doi.org/10.1080/15732479.2019.1605394
UIC(Paris: International Union of Railway), 1994. Guideline for evaluation passenger comfort relation to vibration in railway vehicles. Code 513.
Wei L, Zeng J, Chi MR, et al., 2017. Carbody elastic vibrations of high-speed vehicles caused by bogie hunting instability. *Vehicle System Dynamics*, 55(9), 1321-1342. http://dx.doi.org/10.1080/00423114.2017.1310386
Xiong CB, Lian, SD. 2021. Structural damage identification based on improved fruit fly optimization algorithm. *KSCE Journal of Civil Engineering*, 25(3), 985-1007.
You TW, Gong D, Zhou JS, et al., 2021. Frequency response function-based model updating of flexible vehicle body using experiment modal parameter. *Vehicle System Dynamics*, 60(11), 3930–3954. https://doi.org/10.1080/00423114.2021.1983182
Zhu HP, Li, JJ, Tian W, et al., 2021. An enhanced substructure-based response sensitivity method for finite element model updating of large-scale structures. *Mechanical Systems and Signal Processing*, 154, 107359. https://doi.org/10.1016/j.ymssp.2020.107359 https://doi.org/10.1007/s12205-021-1115-5
Zhang XY, Jin XL, Qi WG, et al. 2008. Vehicle crash accident reconstruction based on the analysis 3D deformation of the auto-body. *Advances in Engineering Software*, 39(6), 459-465. https://doi.org/10.1016/j.advengsoft.2007.05.002
Zhai WM. 2019. Vehicle-track coupled dynamics: theory and applications. Singapore: Springer Nature. (in Chinese)

Unedited

中文概要

题　目：高速列车车体柔性共振有限元模型修正方法及其应用研究

作　者：昌超[1,2,3]，凌亮[2]，马晓毅[1]，李凡松[2]，刘涛[3]，翟婉明[2]

机　构：[1]华东交通大学，机电与车辆工程学院，中国南昌，330013；[2]西南交通大学，轨道车辆系统国家重点实验室，中国成都，610031；[3]中车长春轨道客车股份有限公司，中国长春，130000

目　的：高速列车车体柔性共振现象对高速列车的稳定性和安全性影响极大。因此，建立精确的有限元模型对构建刚柔多体动力学模型、揭示高速列车柔性共振机理至关重要。本文基于实验模态分析，提出一种有效的高速列车车体有限元模型校准与验证方法，通过建立考虑实际约束的详细三维车体有限元模型，结合遗传算法优化车体材料参数，最终基于修正模型建立高速列车车辆－轨道刚柔耦合动力学模型，以准确复现现场观测到的车体柔性共振现象和弹性模态频率。从而为高速列车车体异常抖动机理研究和运行安全提升提供可靠理论依据。

创新点：1. 结合实验模态分析与遗传算法，提出针对高速列车车体的有限元模型修正方法，实现了材料参数的精准优化；2. 建立考虑实际约束的详细三维车体有限元模型，纳入车体附属设备及连接方式对模态特性的影响，提升了模型的真实性；3. 将修正后的有限元模型应用于车辆－轨道耦合动力学分析，成功复现车体柔性共振现象，验证了模型在动态响应模拟中的有效性，为车体柔性振动问题的研究提供了新的技术路径。

方　法：1. 构建三维车体有限元模型：考虑车体铝合金外壳、内部配件及底部设备，采用壳单元、梁单元、质量单元等模拟不同结构，定义材料参数并进行初始模态分析（表 1、图 5）；2. 开展车体模态试验：通过电振动台施加随机激励，布置 196 个测点采集振动信号，采用 PolyMAX 方法识别模态参数（频率、振型、阻尼比），并通过 MAC、MPC 指标验证试验有效性（图 6-8）；3. 模型修正与优化：基于拉丁超立方抽样进行灵敏度分析，筛选对模态响应影响显著的参数（弹性模量、密度），以遗传算法优化参数，使数值模态与实验模态的频率误差小于 5%、MAC 值大于 0.8（图 9-12）；4. 动力学模型应用：基于修正后的车体模型建立车辆－轨道刚柔耦合动力学模型，模拟正常运行及共振工况下的动态响应，并与现场实测数据对比，验证模型对柔性共振的复现能力（图 13-15）。

结　论：1. 修正后的有限元模型在模态参数模拟上与实验结果高度一致，频率误差显著降低，MAC 指标提升，表明模型能准确反映车体动态特性；2. 基于修正模型的车辆－轨道耦合动力学模型，其动态响应（如加速度时程、功率谱密度）与现场实测数据吻合良好，可有效复现车体柔性共振现象；3. 该模型修正方法为高速列车车体柔性振动分析及共振问题解决提供了可靠的数值工具，可进一步用于故障识别和优化设计。

关键词：高速列车；车体柔性共振；有限元；模型修正；模态频率